

Article

Fabrication of $\text{La}_2\text{O}_3/\text{g-C}_3\text{N}_4$ Heterojunction with Enhanced Photocatalytic Performance of Tetracycline Hydrochloride

Zhengru Zhu ¹, Haiwen Xia ¹ , Rina Wu ^{1,*}, Yongqiang Cao ¹ and Hong Li ²

¹ School of Geography, Liaoning Normal University, Dalian 116029, China; zhengruzhu@lnnu.edu.cn (Z.Z.); haiwen1997@126.com (H.X.); caoyongqiang@lnnu.edu.cn (Y.C.)

² Department of Basic, Dalian Naval Academy, Dalian 116018, China; lswlx903@163.com

* Correspondence: wurina@lnnu.edu.cn; Tel.: +86-0411-82159593

Abstract: In this study, $\text{La}_2\text{O}_3/\text{g-C}_3\text{N}_4$ heterojunction photocatalysts doped with different dosages of La_2O_3 were constructed by a facile ultrasound-assisted calcination approach. The as-prepared photocatalysts were characterized by XRD, FTIR, FESEM, TEM, XPS, PL and DRS to verify the composite photocatalysts' purity and to investigate their structural, morphological and elemental composition, and their energy band. According to the results, a type of pure rod-sheet-shaped, heterostructured nanoparticle was successfully obtained. Decorated with 10% La_2O_3 , 2 g/L of the composite sample had a 93% degradation rate for 20 mg/L tetracycline hydrochloride within 2 h under visible light at a pH of 7. After four successive photocatalytic runs, satisfactory stability and reusability was exhibited, with 70% of the tetracycline hydrochloride being removed in the final experiment. Electrons (e^-), photogenerated holes (h^+), superoxide radical anions ($\cdot\text{O}_2^-$) and hydroxyl radicals ($\cdot\text{OH}$) were the fundamental active species during the photocatalytic process and were investigated via quenching experiments. Furthermore, possible photocatalytic mechanisms were analyzed in this work.

Keywords: $\text{La}_2\text{O}_3/\text{g-C}_3\text{N}_4$; heterojunction; photocatalytic performance; tetracycline hydrochloride



Citation: Zhu, Z.; Xia, H.; Wu, R.; Cao, Y.; Li, H. Fabrication of $\text{La}_2\text{O}_3/\text{g-C}_3\text{N}_4$ Heterojunction with Enhanced Photocatalytic Performance of Tetracycline Hydrochloride. *Crystals* **2021**, *11*, 1349. <https://doi.org/10.3390/cryst11111349>

Academic Editors: Dmitri Donetski and Giuseppe Greco

Received: 1 October 2021

Accepted: 4 November 2021

Published: 5 November 2021

Publisher's Note: MDPI stays neutral with regard to jurisdictional claims in published maps and institutional affiliations.



Copyright: © 2021 by the authors. Licensee MDPI, Basel, Switzerland. This article is an open access article distributed under the terms and conditions of the Creative Commons Attribution (CC BY) license (<https://creativecommons.org/licenses/by/4.0/>).

1. Introduction

In the past decades, a multitude of unprecedented materials have been fabricated, and subsequently entered the environment, throughout the process of scientific and technological development. Most of them cannot be decomposed naturally. Faced with this scenario, mankind's sustainable development is at risk of crisis, and green development must be put on the agenda. At the same time, methods for easing environmental pollution have attracted tremendous attention. Scientists have been looking for green, convenient, efficient, fast and low-cost methods to solve the problem of environmental pollution. Fortunately, photocatalysts have been used to degrade pollution from heavy metals, dyes and organic compounds since the proposal of the "Honda-Fujishima Effect" in 1972 [1,2]. Following this, metal oxides, metal sulfides and noble metal semiconductors were selected to be the "cleaner" of organic pollutants, such as TiO_2 and the like. However, this type of photocatalyst only takes effect under ultraviolet light irradiation with wavelengths shorter than 400 nm [3,4]. The high costs and inefficiency of this method has spurred further research to find an ideal photocatalyst. From this point onward, more and more photocatalytic materials, sensitive under visible light, have been discovered. For example, Sheng et al. reported that Fe_2O_3 had a 66% photodegradation efficiency for MB over a period of 120 min with the assistance of visible light [5]; Liang et al. degraded 74.2% of Orange II under 120 min of visible light by using a CdS photocatalyst [6]; and Meng et al. employed a Bi_2WO_6 photocatalyst to remove 95% of Rhb while exposed to 60 min of visible light [7].

Graphite carbon nitride ($\text{g-C}_3\text{N}_4$), a novel polymeric semiconductor photocatalyst, has received a great deal of focus in recent years. In 2009, Xinchun et al. proposed it for use in hydrogen production from water under visible light [8]. It has simple synthesis steps, a low

cost, and it has stable chemical properties. However, as a photo-generated carrier it is short-lived, it has low photocatalytic efficiency under visible light and other flaws restraining its degradation efficiency [9,10]. Many approaches have been proposed to solve these problems, such as element doping, morphological control and so on [11–13]. Modifying the photocatalyst to be a heterojunction was found to be an efficient means to enhance the visible light utilization of g-C₃N₄ and control its cost. Heterojunction-based g-C₃N₄ were fabricated, such as Fe₂O₃/g-C₃N₄, ZnO/g-C₃N₄, MnO₂/g-C₃N₄ and so on. ShuYao et al. synthesized Fe₂O₃/g-C₃N₄ and found that it had a removal rate of 92% for basic fuchsin degradation after 210 min [14]. Jia-Xin et al. decorated g-C₃N₄ with ZnO, which led to the decomposition of 97% of MO in 80 min under visible light [15]. Panimalar et al. eliminated 98% of phenol dyes with a MnO₂/g-C₃N₄ heterojunction photocatalyst in 100 min [16]. All of the heterojunction photocatalysts noted above are conventional metal oxides loaded on g-C₃N₄ with higher degradation efficiency compared to pristine metal oxides and g-C₃N₄. Lanthanum is a rare earth element that has the significant ability to improve the photocatalytic effects recorded in previous reports. Loan et al. decorated ZnO with La and its photocatalytic performance was approximately 50% higher than that of pure ZnO [17]. Wen et al. modified ZnIn₂S₄ with LaFeO₃ to remove MO, and the degradation rate increased by 59% [18]. These results indicate that La and its compounds are advantageous in improving photocatalytic performance, no matter the element loading or heterojunction modification. Therefore, the La₂O₃/g-C₃N₄ heterojunction photocatalyst was proposed for investigation in this work and expected to provide solutions to existing practical problems. Tetracycline Hydrochloride (TTCH), an antibiotic widely present in the natural environment due to excessive human use, was selected as the chemical compound to be targeted during evaluation of the degradation performance of the La₂O₃/g-C₃N₄ heterojunction photocatalyst.

To sum up, different assembled amounts of La₂O₃/g-C₃N₄ samples were prepared and evaluation of their photocatalytic performance in degrading TTCH under visible light irradiation was performed. Moreover, the possible photodegradation mechanism is discussed in this work.

2. Materials and Methods

2.1. Materials

All the chemicals were reagent grade, provided by Sinopharm Chemical Reagent Co. (Shanghai, China) and used without further purification.

2.2. Synthesis of Nanocomposites

Using the method established in previous reports, pristine g-C₃N₄ was prepared by one-step calcination. A covered ceramic crucible was filled with 5 g of melamine and was heated to 550 °C in a muffle furnace for 2 h, with a heating rate of 5 °C/min. After cooling and grinding, the faint yellow powdered g-C₃N₄ was prepared and marked as CN [19].

Per the directions in the relevant studies, 2 g of LaN₃O₉·6H₂O was placed in a covered ceramic crucible and heated to 720 °C in a muffle furnace for 2 h, with a heating rate of 10 °C/min. Once cooled to room temperature, the precursor was ground into a powder. The obtained La₂O₃ sample was named LaO [20].

La₂O₃/g-C₃N₄ heterojunction composite photocatalysts were synthesized by an ultrasound-assisted calcination approach. Per traditional methodology, the g-C₃N₄ powder was dispersed in 10 mL of anhydrous ethanol with ultrasonic vibration for 10 min. Then, the appropriate amount of La₂O₃ powder was added into the solution. The resulting mixture was put into a vacuum drying oven at 80 °C for 12 h and then heated at 320 °C in a muffle furnace for 2 h to remove impurities. Finally, the La₂O₃/g-C₃N₄ samples (with loads of 5%, 10%, 15% and 20%) were obtained, which were labeled as 5LaO/CN, 10LaO/CN, 15LaO/CN and 20LaO/CN, respectively [21].

2.3. Characterization

An X-ray diffractometer (Shimadzu, Kyoto, Japan) equipped with Cu K α radiation was employed to obtain the crystal structure and phase composition of the photocatalyst samples. The Fourier transform infrared spectrum (FTIR) of the photocatalysts was measured by a TENSOR 27 FTIR spectrometer (Bruker AXS, Karlsruhe, Germany). The size and morphological properties of LaO, CN and 10LaO/CN were observed by SU8010 field emission scanning microscopy (Hitachi, Tokyo, Japan) and JEM-2100 transmission electron microscopy (JEOL, Tokyo, Japan). The X-ray photoelectron spectroscopy (XPS) was characterized by using an ESCALAB250 multifunctional surface analysis system (Thermo VG, MA, USA) and then a Lambda 35 UV-Visible Spectrophotometer (PerkinElmer, MA, USA) was applied to determine binding energies. The photoluminescence spectra (PL) were obtained by an RF-540 Fluorescence Spectrophotometer (Shimadzu, Kyoto, Japan).

2.4. Photocatalytic Activity Test

In order to inspect the effect of the compounding concentration on photocatalytic activity, the TTCH was degraded with bare CN, pristine LaO, 5LaO/CN, 10LaO/CN, 15LaO/CN and 20LaO/CN under visible light ($\lambda \geq 400$ nm). Per the usual protocol, these were tested on 50 mL of suspension which contained TTCH (20 mg/L) and CN powders dispersed by an ultrasonic machine. The suspension was stirred in the dark until the absorption-desorption equilibrium was attained. The fluid was then sampled every 20 min and the absorbance data at 356 nm were recorded.

The active species were observed to further demonstrate the mechanism of photocatalytic degradation. Anhydrous ethanol (C₂H₆O), silver nitrate (AgNO₃), benzoquinone (BQ) and ethylene glycol (IPA) were used as hole (h⁺) quencher, electron (e⁻) quencher, hydroxyl radical (\cdot OH) quencher and superoxide radical (O₂⁻) quencher, respectively.

3. Results and Discussion

3.1. XRD Analysis

The crystalline phase of the as-prepared samples was investigated by XRD, as shown in Figure 1. Distinct diffraction peaks of the CN pattern can be observed, located at 27.48° which corresponds to the (002) crystal planes of standard XRD cards for g-C₃N₄ (JCPDS No.87-1526), indicating its aromatic rings are stacked on the 002 plane [22–24]. The characteristic peaks of LaO valued at 26.16°, 29.15°, 30.01°, 39.57°, 46.15°, 48.62°, 52.23°, 55.53°, 56.04° and 75.45° were matched to the (100), (002), (011), (012), (110), (111), (103), (112), (021) and (211) crystal planes of the standard XRD cards for La₂O₃ (JCPDS No.74-1144), respectively [20]. Regarding composite sample patterns, the (002) and (011) peaks of LaO were detected at 29.37° and 30.36°, respectively. The (002) peak of CN in composite samples indexed to 27.7° [25]. All these peaks had a slight red-shift and demonstrated the heterojunction formed between the (002) facet of CN and the (011) facet peak of LaO, which further illustrated that the heterojunction photocatalysts were fabricated successfully [26]. In addition, there were no other miscellaneous peaks on the spectrum, indicating that the sample was relatively pure.

3.2. FESEM and TEM Analysis

In order to investigate the surface microstructure and morphology, the microscopic details of the samples were obtained using FESEM and TEM analyses, as shown in Figure 2. As observed in Figure 2a, numerous CN nanosheets were superimposed upon one another. Plentiful rod-like LaO nanoparticles were clustered together, as evidenced in Figure 2b. After compounding, the LaO nanoparticles were deposited on lamellar CN and they recombined into close-knit polymers as clearly seen in Figure 2c,d. These results further confirmed that heterojunction structures formed between LaO and CN.

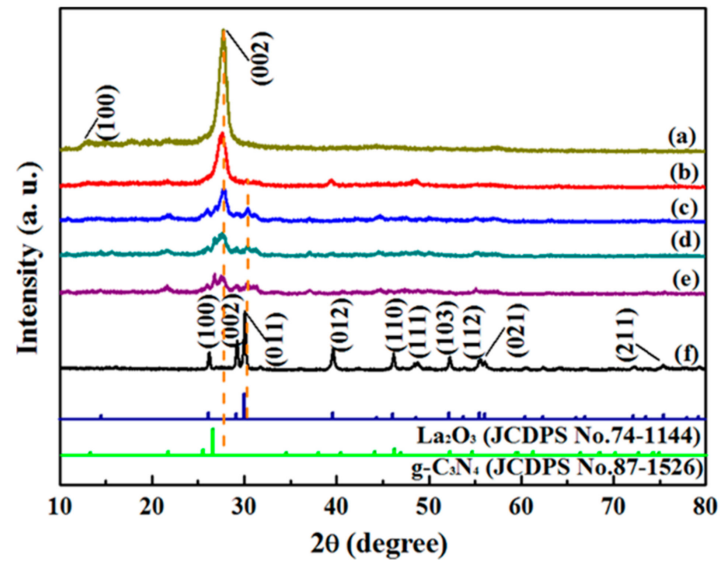


Figure 1. XRD patterns of CN (a), 5LaO/CN (b), 10LaO/CN (c), 15LaO/CN (d), 20LaO/CN (e), LaO (f) samples and standard card.

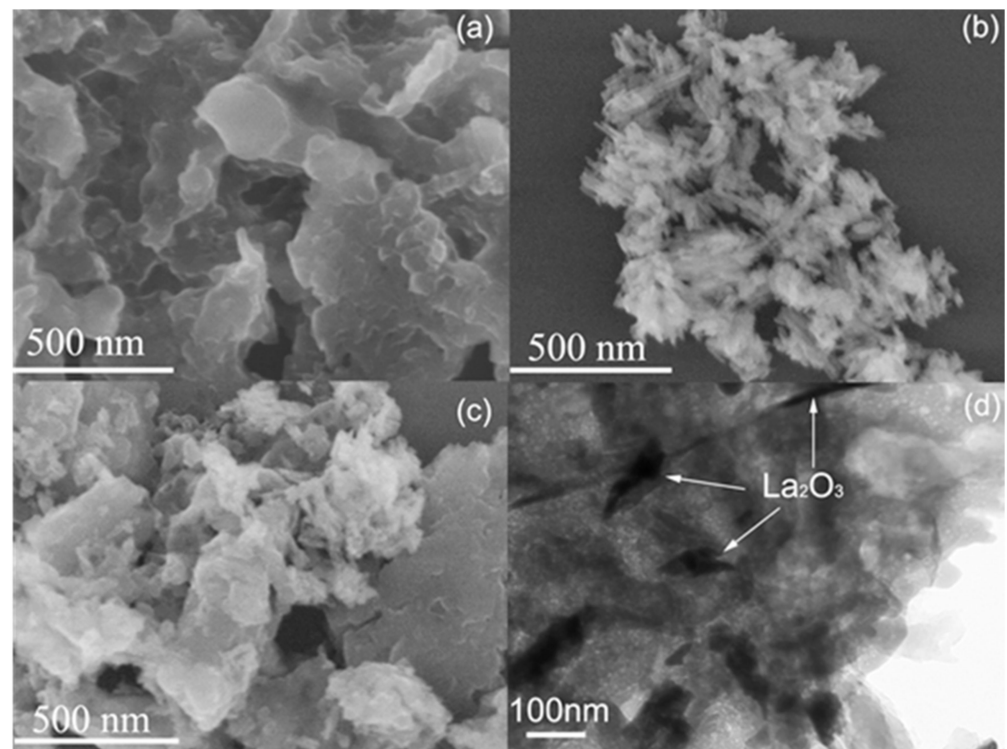


Figure 2. FESEM patterns of CN sample (a), LaO sample (b), 10LaO/CN sample (c), and TEM pattern of 10LaO/CN sample (d).

3.3. FTIR Analysis

The functional groups and vibrational features of the samples, revealed in Figure 3, were elucidated via the use of FTIR. For pristine LaO and bare CN, La–O induced the band to discern at 670 cm^{-1} , while the peak at 781 cm^{-1} was due to triazine units (3-s) [27]. The characteristic bands from 1200 to 1660 cm^{-1} were attributed to the skeletal vibrations of aromatic C–N heterocycles. Several somewhat feeble absorption peaks around 3200 cm^{-1} represented the O–H stretching of the hydroxyl group [28]. In the spectrum of composite samples, the bands valued at 1223 , 1423 , 1556 and 1657 cm^{-1} were similar to CN, indicating

once again that the composite material was successfully prepared. As the graphite phase structure of CN cannot be changed, the reactions only occurred on the surface [29].

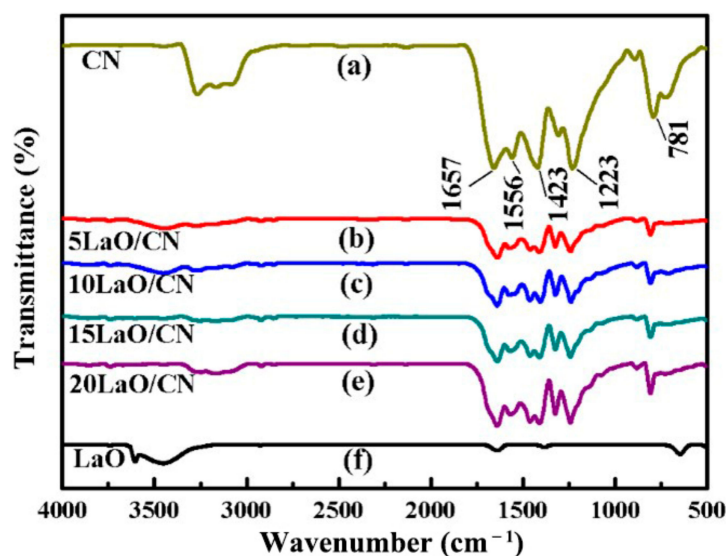


Figure 3. FTIR patterns of CN sample (a), 5LaO/CN sample (b), 10LaO/CN sample (c), 15LaO/CN sample (d), 20LaO/CN sample (e), LaO sample (f).

3.4. XPS Analysis

Figure 4 displays the surface chemical composition of 10LaO/CN. Therein, the survey scan of the XPS spectrum (see Figure 4a) illustrates that the as-tested sample contains lanthanum, oxygen, nitrogen and carbon; the same components as the photocatalyst samples prepared. The detailed full width half maximum (FWHM) is shown in Table 1. As shown in Figure 4b, the peaks located at 284.6 eV and 289.9 eV of C 1s were assigned to sp^2 -hybridised carbon and surface adventitious carbon; the strongest peak, located at 287.8 eV, could be ascribed to carbon atoms bonded with N-containing aromatic rings (N–C=N) [30–32]. The N 1s spectra are exhibited in Figure 4c; a pair of N peaks were distinguished at 398.3 eV and 399.7 eV, assigned to sp^2 hybridized N involved in the triazine rings (C–N=C) and tertiary nitrogen (N–(C₃)), respectively [33–35]. Two peaks in Figure 4d were fitted to the O 1s spectrum at 527.7 eV and 529.7 eV, which corresponds to the hydroxyl groups (O–H) and (O–N), and the latter peak was assigned to the intermediates of melamine [21,36]. As shown in Figure 4e, four peaks were found in the La 3d XPS spectrum of the 10LaO/CN sample. The binding energies at 835.1 eV and 838.8 eV could be ascribed to La 3d_{5/2}. The peak of La 3d_{3/2} was found at 851.8 eV and its satellite peak was found at 855.8 eV [37]. Furthermore, all the peaks of La had reasonable FWHM proportions. These spectra results bear out the coexistence of LaO and CN in composite photocatalysts.

Table 1. Position and full width half maximum.

Composition	Binding Energy (eV)	FWHM (eV)
C 1s	289.9 eV	1.18 eV
	287.8 eV	2.20 eV
	284.6 eV	1.87 eV
O 1s	529.7 eV	2.21 eV
	527.7 eV	1.80 eV
N 1s	399.7 eV	1.47 eV
	398.3 eV	2.01 eV
La 3d _{5/2}	838.8 eV	3.42 eV
	835.1 eV	
La 3d _{3/2}	855.8 eV	3.42 eV
	851.8 eV	

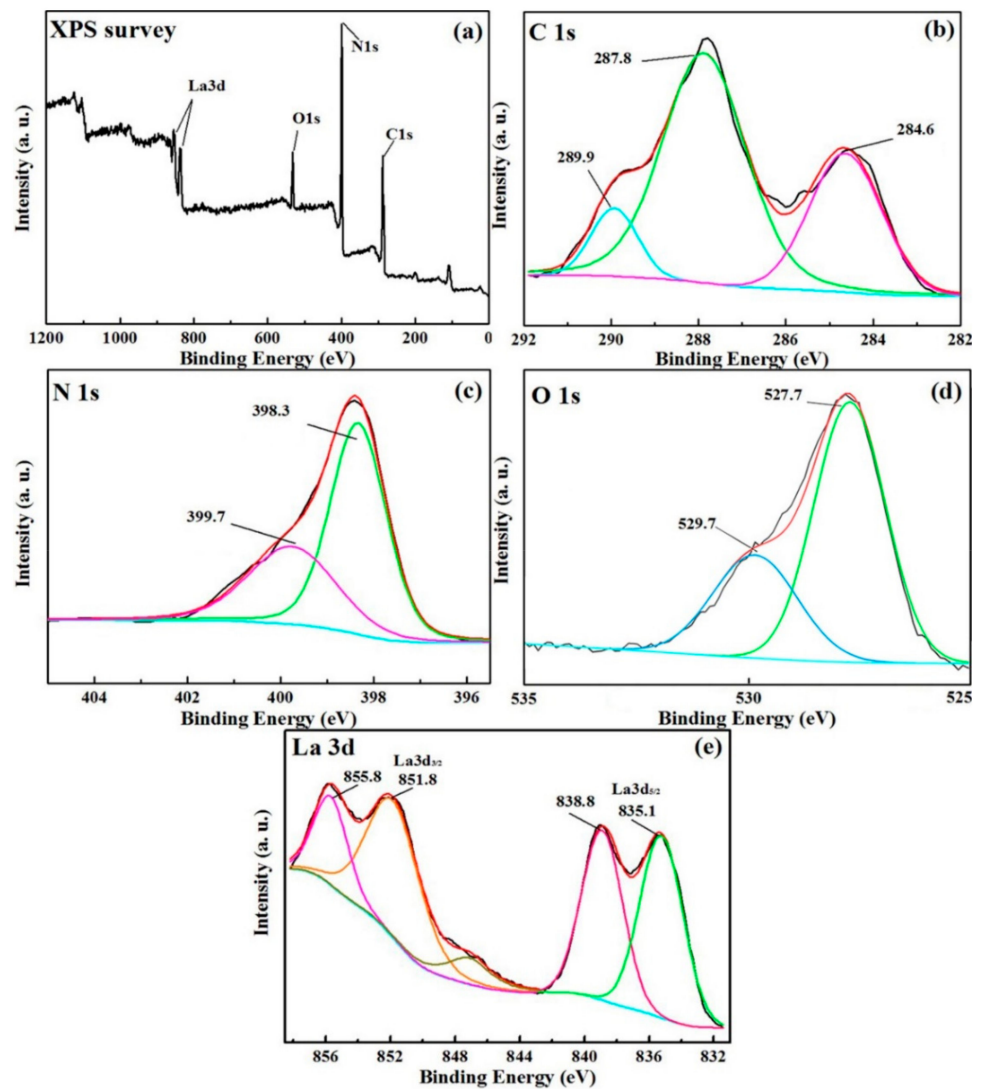


Figure 4. XPS survey pattern of 10LaO/CN (a); the high-resolution XPS spectra of C 1s (b), N 1s (c), O 1s (d) and La 3d (e).

3.5. UV–Vis Analysis

The light utilization capacity of the samples was studied through UV–vis diffuse reflection, and the results are exhibited in Figure 5a. Comparing these to samples without a composite, a slight red-shift could be observed in the spectral line of the composite sample. At the range of 480 to 510 nm, the composite samples had a wider absorption range, and higher absorption level, than CN in visible light. In particular, the absorption edge of 10LaO/CN was the largest. Distinctly, CN coupled with LaO had stronger visible light absorption capacities [38]. The high-efficiency optical absorption capacity and the narrow band gap meant that more active electrons translated from the valence band (VB) to the conduction band (CB). In other words, these samples had powerful photocatalytic performance. As shown in Figure 5b, the band gap of the CN, LaO and 10LaO/CN samples were calculated to be 2.9 eV, 5.28 eV and 2.66 eV, which coincided with the previous estimates [39]. Well-matched valence and conduction band potentials prompted CN and LaO to form a heterojunction. Moreover, abundant notches generated on the surface held back the recombination efficiency of photogenerated electrons and holes to further improve the photocatalytic performance [40].

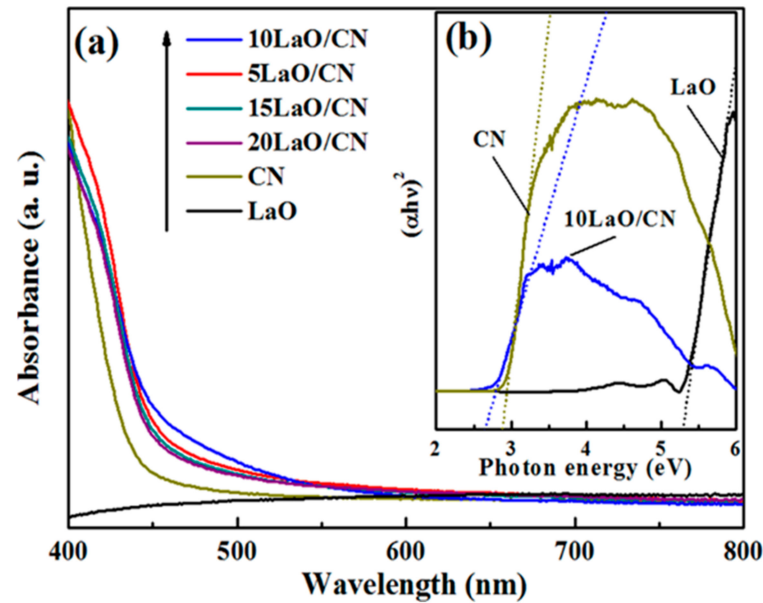


Figure 5. The UV–visible diffuse reflection patterns of LaO, CN, 5LaO/CN, 10LaO/CN, 15LaO/CN and 20LaO/CN (a); inset: plots of the $(\alpha h\nu)^2$ vs. photon energy ($h\nu$) for LaO, CN and 10LaO/CN (b).

3.6. PL Analysis

Figure 6 shows the photogenerated separation and migration of the electrons in the as-prepared photocatalysts. With the excited wavelength at 290 nm, all PL spectra of the compounds and CN exhibited emissions with a band centered at 438 nm. However, LaO had no PL signal in the same condition [41–43]. Typically, lower PL emission intensity correlates with lower recombination efficiency of the photogenerated electrons and holes. Thereby, the 10LaO/CN sample possessed splendid separation and migration efficiency of the photogenerated electrons and holes, the best in all the samples [44,45]. These results were consistent with the conclusions of the UV–vis analysis.

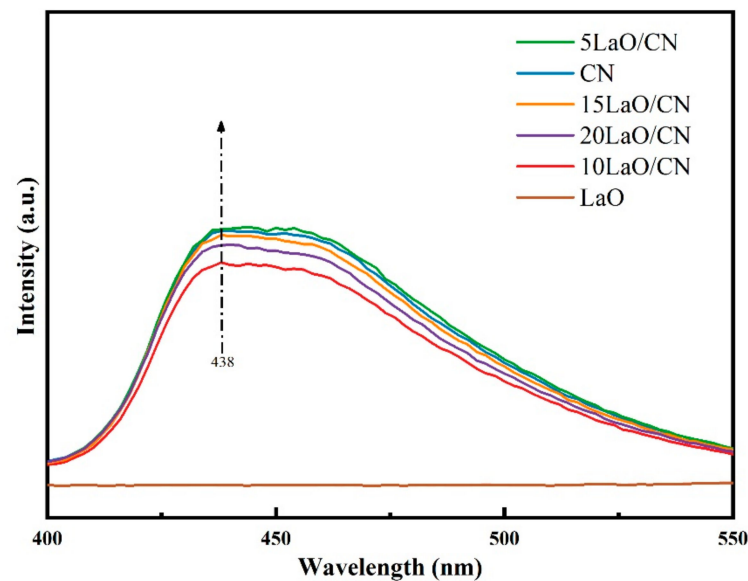


Figure 6. PL emission patterns of CN, 5LaO/CN, 10LaO/CN, 15LaO/CN, 20LaO/CN and LaO samples.

3.7. Photocatalyst Activity

Photocatalytic processes occurred on the surface of the catalysts, and absorption efficiency significantly affected photocatalytic performance [46]. Samples reached the absorption–desorption equilibrium in 30 min, as Figure 7a shows. The LaO/CN heterojunctions absorbed varying amounts of TTCH on their surfaces, facilitating photocatalytic degradation. TTCH only had a 0.2% photolysis rate in the natural environment. Most of TTCH was removed by the composite samples and it had higher photocatalytic activity than CN under visible light irradiation. The most efficient photocatalyst was 10LaO/CN; its degradation rate of TTCH was 93% in 2 h. The comparison between this and the other g-C₃N₄-based heterojunction photocatalysts is shown in Table 2. And the photocatalytic results of all samples were exhibited in Table 3.

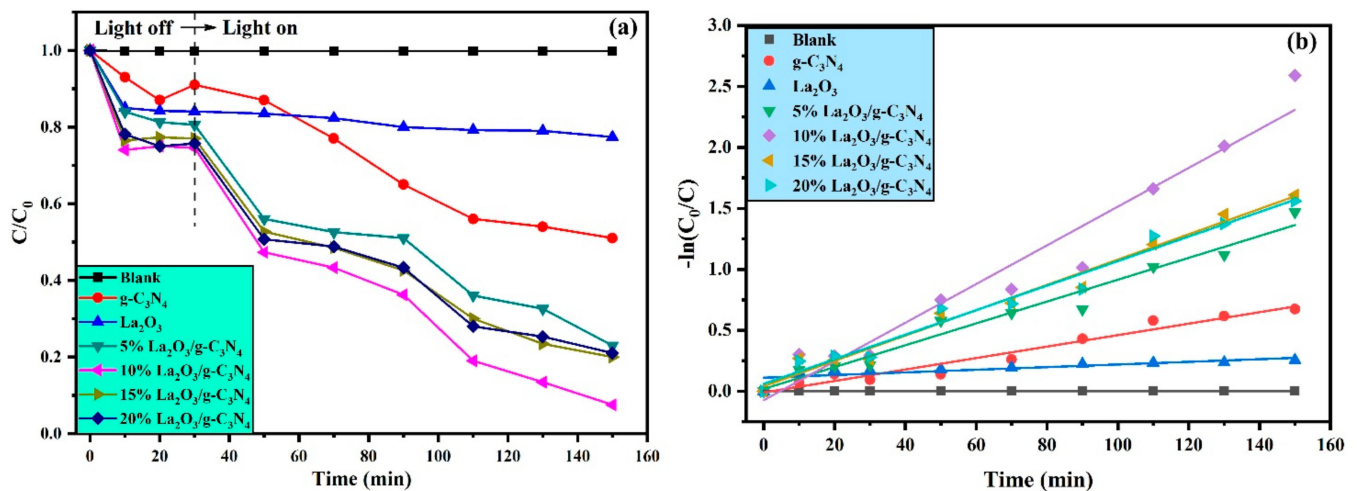


Figure 7. Photocatalytic degradation performance of samples (a); kinetic curves of TTCH degradation (b).

Table 2. Comparison with other g-C₃N₄ based heterojunction photocatalyst in TTCH degradation.

Sample Name	Degradation (%)	Time (Min)	Light Source	Reference
Ag ₂ O/g-C ₃ N ₄	89%	180 min	UV light	[47]
Bi ₂ WO ₆ /g-C ₃ N ₄	73%	105 min	visible light	[48]
Co ₃ O ₄ /g-C ₃ N ₄	73.8%	120 min	visible light	[49]
Nb ₂ O ₅ /g-C ₃ N ₄	73.7%	60 min	visible light	[50]
Sn ₃ O ₄ /g-C ₃ N ₄	72.2%	120 min	visible light	[51]
WO ₃ /g-C ₃ N ₄	82%	120 min	visible light	[52]
ZrO ₂ /g-C ₃ N ₄	90.6%	60 min	visible light	[53]
La ₂ O ₃ /g-C ₃ N ₄	93%	180 min	visible light	This work

Table 3. Photocatalytic results of all samples.

Sample Name	Degradation (%)	K (Min ⁻¹)	R ²
g-C ₃ N ₄	49%	0.00470	0.96022
5% La ₂ O ₃ /g-C ₃ N ₄	77%	0.00896	0.97010
10% La ₂ O ₃ /g-C ₃ N ₄	93%	0.01588	0.95393
15% La ₂ O ₃ /g-C ₃ N ₄	80%	0.01039	0.98064
20% La ₂ O ₃ /g-C ₃ N ₄	79%	0.01007	0.97583

The kinetic curves of TTCH degradation in the samples were linearly fitted to a first-order model and are shown in Figure 7b. The kinetic constants of LaO, CN, 5LaO/CN, 10LaO/CN, 15LaO/CN and 20LaO/CN were 0.00108, 0.00470, 0.00896, 0.01588, 0.01039 and 0.01007 min⁻¹, respectively. The reaction rate of 10LaO/CN was 1.89 times that of CN and 4.11 times that of pristine LaO.

TOC was measured to test the mineralization degree of organic pollutants in the water during the degradation process, and then the final degraded solution was filtered and tested. After degradation with 10LaO/CN, the residual TOC was about 4.61 mg/L. Evidently, most of the TTCH in the solution was degraded and mineralized.

For optimum experimental conditions, factors that might influence the results of the experiment must be controlled. The amount of the photocatalyst was an important factor in catalytic activity. As Figure 8a depicts, the photocatalytic degradation ratio of the 10LaO/CN sample for TTCH reached 68.6%, 78.8%, 93% and 78.9% for 0.5 g/L, 1 g/L, 2 g/L and 4 g/L of photocatalysts, respectively. As expected, the best degradation effect was found in the 2 g/L of photocatalyst sample.

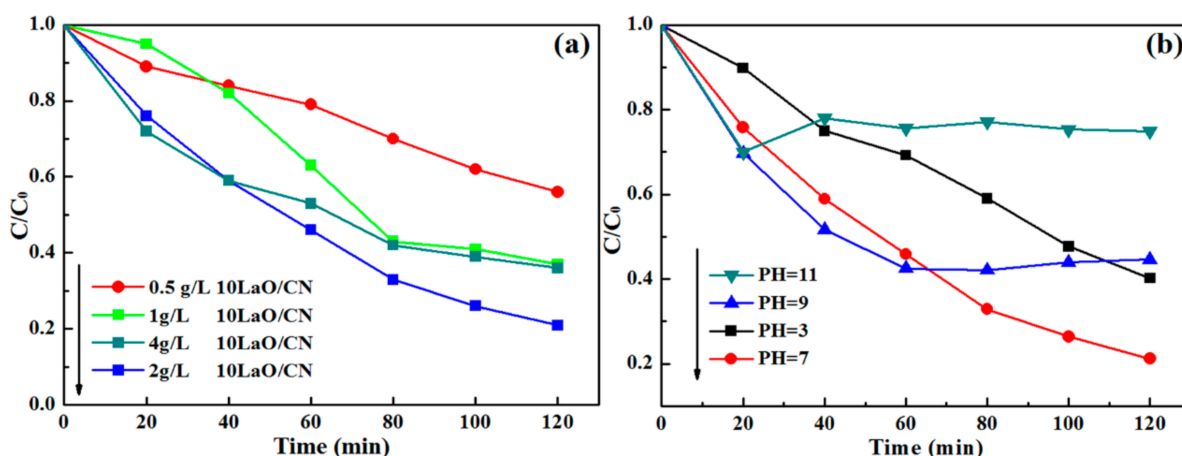


Figure 8. Different factors influencing photocatalytic activities for 10LaO/CN degraded TTCH: different concentration (a); pH value (b).

Similarly, pH was another factor affecting the experimental data. The pH levels of the TTCH solutions were 3, 7, 9 and 11 (± 0.1), respectively. As shown in Figure 8b, photocatalytic activity was not improved in an acid solution (with a pH of 3). After adjusting the solution's pH to 11, photocatalytic activity was significantly inhibited. When the pH was set to 9, TTCH was removed quickly over the span of an hour before reaching a stable concentration. Overall, the pH of the solution tended to be neutral during the process of degradation. Working against this was the fact that TTCH decreased steadily in a neutral solution. For performance reasons, the TTCH solution is best maintained at a pH of 7.

The optimal experimental conditions were set in a chemical oxygen demand tester (COD) expedited testing apparatus. When the pH was equal to 7, 0.1 g of the 10LaO/CN sample degraded 82.2% of COD for the TTCH solution in 2 h. The experimental results suggest that organics were effectively shed by composite heterojunction photocatalysts.

3.8. Stability and Active Species

The application of the 10LaO/CN sample in cyclic experiments verified its stability. Figure 9a shows the results of four successive rounds of experimentation, in which the 10LaO/CN sample could still degrade 70% of the TTCH in the final test. The slight decrease in photocatalytic activity was due to the products absorbed by the active sites of the catalyst. This result demonstrates that the photocatalytic activities of photocatalysts still remain effective. In Figure 9b, the results of the XRD analysis carried out after the cyclic experiments indicate that the crystal structure and phase composition of the 10LaO/CN photocatalyst was basically unchanged in the photocatalytic process. Hence, the 10LaO/CN sample had good stability after four cycles.

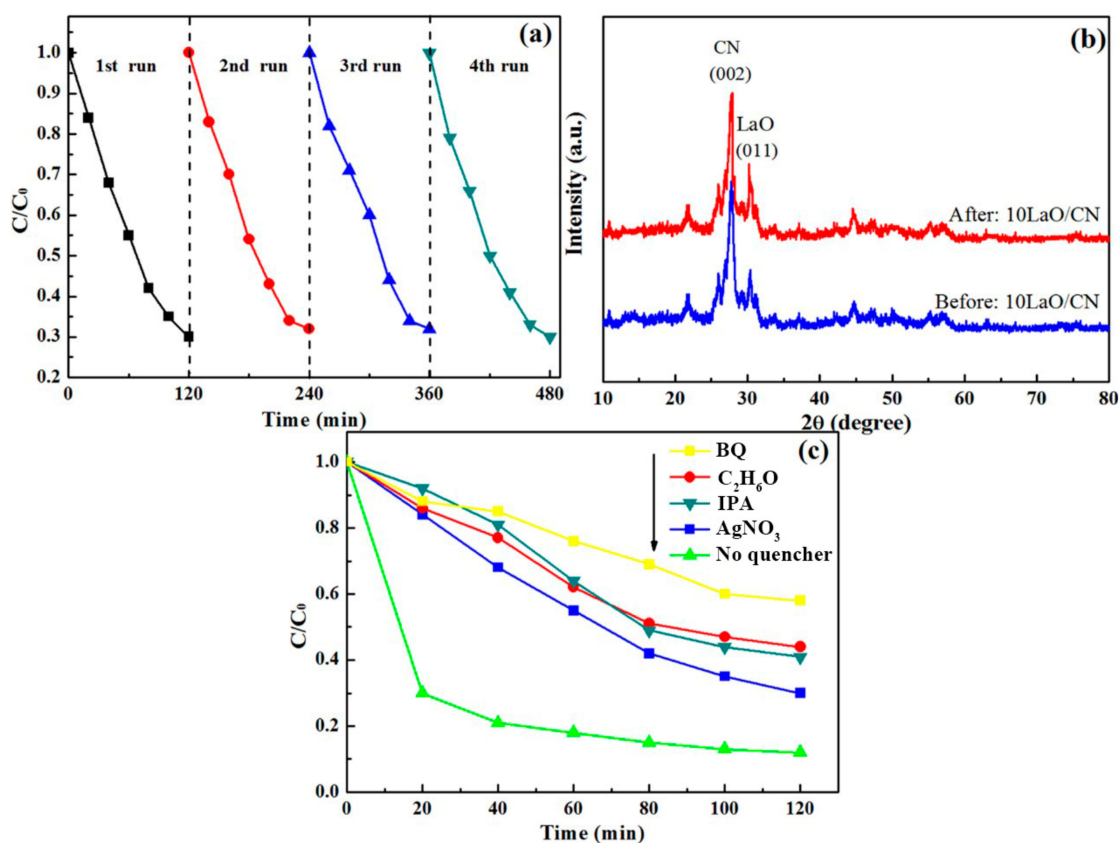


Figure 9. Reusability of photocatalytic activities experiment on 10LaO/CN photocatalysts (a); XRD patterns of 10LaO/CN before and after the degradation of TTCH (b); the effect of active species in TTCH degradation (c).

Various kinds of quenchers were used to test the effect of active species on TTCH degradation. As shown in Figure 9c, the heterojunction still maintains high degradation efficiency with no quencher. However, when the e^- , h^+ , O_2^- or OH were removed with quenchers, the degradation efficiency was distinctly decreased. Therefore, e^- , h^+ , O_2^- and OH were the main active substances participating in the process of degrading TTCH.

3.9. Photocatalytic Reaction Mechanism

In the photocatalytic process, the efficiency of the photo-induced electrons' (e^-) migration determines the photocatalytic performance; hence, it was necessary to appraise the relevant band positions. As shown in Figure 10, after the composite photocatalyst was excited by visible light, the electrons absorbed abundant energy and leapt from the valance bands (VB) of LaO and CN to the conduction bands (CB) of LaO and CN. Photoinduced electrons were concentrated in the CB, and photogenerated holes (h^+) were distributed in the VB. In accordance with the theory of absolute electronegativity [54–56], the E_{CB} and E_{VB} of CN were calculated to be -1.22 eV and 1.68 eV and those of LaO were found to be -4.83 eV and 0.45 eV. As previously substantiated in prior research, LaO and CN belong to p-type and n-type semiconductors, respectively [57,58]. In general, the Fermi levels of p-type and n-type semiconductors are located close to the VB and CB, respectively. After the p–n heterojunction is formed, their Fermi energy levels increase until equilibrium is reached. At the same time, their energy bands ascend and descend as Fermi levels move, as shown in Figure 10 [59]. After the composite photocatalyst was excited by visible light, the electrons in the VB of CN absorbed abundant energy and leapt to the CB. However, LaO has a large energy band gap around 5.28 eV and cannot generate electron–hole pairs under visible light irradiation. Photoinduced electrons and holes (h^+) were concentrated in the CB and VB of CN, respectively. Then, the CB of CN and the VB of LaO were adjacent and the VB of LaO was slightly lower, and the photogenerated

electrons on the CB of CN were transferred to the VB of LaO. This extended distance reduced the recombination efficiency of photogenerated electron–hole pairs. Therefore, the lifetimes of the e^- and h^+ were greatly extended and, in turn, increased the efficiency of the photocatalysis process. Additionally, after the heterojunction was formed, the VB of LaO had less than $O_2/\bullet O_2^-$ (-0.046 eV vs. NHE), therefore, the electrons could react with O_2 in the solution and form O_2^- [60,61]. Meanwhile, the VB of CN had higher levels than $\bullet OH/OH^-$ (1.99 eV vs. NHE) and $H_2O/\bullet OH$ ($+2.27$ eV vs. NHE), allowing OH^- and H_2O to form $\bullet OH$ [62]. As shown in the quenching experiments, O_2^- and OH played the main roles in photocatalytic behavior. The long-acting e^- and h^+ produced more active substances and the photocatalytic efficiency improved naturally. Eventually, the TTCH was broken down into H_2O , CO_2 and other products [63,64].

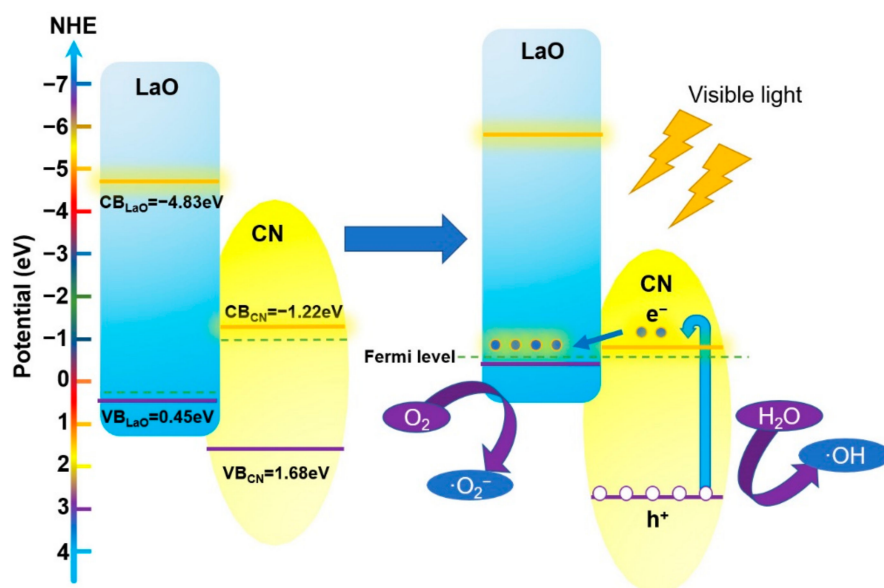


Figure 10. Possible mechanism of LaO/CN composite photocatalyst.

4. Conclusions

$La_2O_3/g-C_3N_4$ heterojunction photocatalysts were synthesized via an ultrasonic method. Compared to pristine $g-C_3N_4$, $La_2O_3/g-C_3N_4$ had higher degradation rates. Specifically, the sample doped with 10% La_2O_3 had a 93% degradation rate for Tetracycline Hydrochloride when exposed to 2 h of visible light. This rate was 1.89 times greater than that of pristine $g-C_3N_4$, and 4.11 times greater than that of pristine La_2O_3 . Clearly, the strong oxidation products of h^+ and OH facilitated the degradation of Tetracycline Hydrochloride. The low recombination of electrons and holes between interfaces also improved photocatalytic efficiency. In summary, the $La_2O_3/g-C_3N_4$ heterojunction photocatalyst is a promising photocatalytic material for environmental purification and is worthy of further research.

Author Contributions: Supervision, H.L. and Y.C.; visualization, R.W.; writing—original draft, H.X.; writing—review and editing, Z.Z. All authors have read and agreed to the published version of the manuscript.

Funding: This research was funded by the National Natural Science Foundation of China (No. 52079060) and the Liaoning Revitalization Talents Program.

Institutional Review Board Statement: Not applicable.

Informed Consent Statement: Not applicable.

Data Availability Statement: Not applicable.

Conflicts of Interest: The authors declare no conflict of interest.

References

1. Fujishima, A.; Honda, K. Electrochemical Photolysis of Water at a Semiconductor Electrode. *Nature* **1972**, *238*, 37–38. [[CrossRef](#)] [[PubMed](#)]
2. Chen, S.; Takata, T.; Domen, K. Particulate photocatalysts for overall water splitting. *Nat. Rev. Mater.* **2017**, *2*, 1704376. [[CrossRef](#)]
3. Adenuga, D.O.; Tichapondwa, S.M.; Chirwa, E.M. Facile synthesis of a Ag/AgCl/BiOCl composite photocatalyst for visible—light—driven pollutant removal. *J. Photochem. Photobiol. A Chem.* **2020**, *401*, 112747. [[CrossRef](#)]
4. Hunge, Y.M.; Yadav, A.A.; Mathe, V.L. Oxidative degradation of phthalic acid using TiO₂ photocatalyst. *J. Mater. Sci. Mater. Electron.* **2018**, *29*, 6183–6187. [[CrossRef](#)]
5. Guo, S.; Zhang, G.; Wang, J. Photo-Fenton degradation of rhodamine B using Fe₂O₃–Kaolin as heterogeneous catalyst: Characterization, process optimization and mechanism. *J. Colloid Interface Sci.* **2014**, *433*, 1–8. [[CrossRef](#)]
6. An, L.; Wang, G.; Zhao, L.; Zhou, Y.; Gao, F.; Cheng, Y. Hexagonal pencil-like CdS nanorods: Facile synthesis and enhanced visible light photocatalytic performance. *Russ. J. Phys. Chem. A* **2015**, *89*, 1195–1200. [[CrossRef](#)]
7. Shang, M.; Wang, W.; Sun, S.; Zhou, L.; Zhang, L. Bi₂WO₆ Nanocrystals with High Photocatalytic Activities under Visible Light. *J. Phys. Chem. C* **2008**, *112*, 10407–10411. [[CrossRef](#)]
8. Wang, X.; Maeda, K.; Thomas, A.; Takanabe, K.; Xin, G.; Carlsson, J.M.; Domen, K.; Antonietti, M. A metal-free polymeric photocatalyst for hydrogen production from water under visible light. *Nat. Mater.* **2008**, *8*, 76–80. [[CrossRef](#)]
9. Liu, J.; Qiu, L.; Chang, M.-J.; Yuan, B.; Sun, M.; Fan, S.-M.; Cui, W.-N.; Hui, Q.; Ni, F.-R.; Li, M.-Y.; et al. Fabrication of novel fibrous BiVO₄/CdS heterostructures by electrospinning method for efficient visible light photodegradation. *Mater. Chem. Phys.* **2020**, *247*, 122858. [[CrossRef](#)]
10. Darvishi-Farash, S.; Afsharpour, M.; Heidarian, J. Novel siligraphene/g-C₃N₄ composites with enhanced visible light photocatalytic degradations of dyes and drugs. *Environ. Sci. Pollut. Res.* **2020**, *28*, 5938–5952. [[CrossRef](#)]
11. Kadam, S.R.; Ghosh, S.; Bar-Ziv, R.; Bar-Sadan, M. Structural Transformation of SnS₂ to SnS by Mo Doping Produces Electro/Photocatalyst for Hydrogen Production. *Chem.—A Eur. J.* **2020**, *26*, 6679–6685. [[CrossRef](#)]
12. Kaviyarasan, K.; Sivasankar, T.; Ponnusamy, V.K.; Anandan, S. Ni–ZnO nanocomposites assembled under various morphologies like columnar, nanochains, and granular structure for removal of pollutants. *Mater. Chem. Phys.* **2020**, *252*, 123299. [[CrossRef](#)]
13. Zhu, Z.; Han, S.; Cao, Y.; Jiang, J. Synthesis of a Novel Photocatalyst MVO₄/g-C₃N₄ (M = La, Gd) with Better Photocatalytic Activity for Tetracycline Hydrochloride Degradation under Visible-Light Irradiation. *Crystals* **2021**, *11*, 756. [[CrossRef](#)]
14. Xiong, S.; Liu, X.; Zhu, X.; Liang, G.; Jiang, Z.; Cui, B.; Bai, J. One-step preparation of well-dispersed spindle-like Fe₂O₃ nanoparticles on g-C₃N₄ as highly efficient photocatalysts. *Ecotoxicol. Environ. Saf.* **2020**, *208*, 111519. [[CrossRef](#)]
15. Sun, J.-X.; Yuan, Y.-P.; Qiu, L.-G.; Jiang, X.; Xie, A.-J.; Shen, Y.-H.; Zhu, J.-F. Fabrication of composite photocatalyst g-C₃N₄–ZnO and enhancement of photocatalytic activity under visible light. *Dalton Trans.* **2012**, *41*, 6756–6763. [[CrossRef](#)]
16. Panimalar, S.; Uthrakumar, R.; Selvi, E.T.; Gomathy, P.; Inmozhi, C.; Kaviyarasu, K.; Kennedy, J. Studies of MnO₂/g-C₃N₄ heterostructure efficient of visible light photocatalyst for pollutants degradation by sol-gel technique. *Surf. Interfaces* **2020**, *20*, 100512. [[CrossRef](#)]
17. Nguyen, L.T.T.; Duong, A.T.T.; Nguyen, B.D.; Hai, N.Q.; Chu, V.H.; Nguyen, T.D.; Bach, L.G. Preparation, Characterization and Photocatalytic Activity of La-Doped Zinc Oxide Nanoparticles. *Materials* **2019**, *12*, 1195. [[CrossRef](#)]
18. Gao, W.; Zhang, C.; Cui, S.; Liang, Q.; Xu, S.; Li, Z. In situ Synthesis of p–n LaFeO₃/ZnIn₂S₄ Heterojunctions for Enhanced Photocatalytic Activity. *Nano* **2019**, *14*, 1950096. [[CrossRef](#)]
19. Yan, S.C.; Li, Z.S.; Zou, Z.G. Photodegradation Performance of g-C₃N₄ Fabricated by Directly Heating Melamine. *Langmuir* **2009**, *25*, 10397–10401. [[CrossRef](#)]
20. Li, C.; Hu, R.; Qin, L.; Ding, R.; Li, X.; Wu, H. Enhanced photocatalytic activity of ZnO/La₂O₃ composite modified by potassium for phenol degradation. *Mater. Lett.* **2013**, *113*, 190–194. [[CrossRef](#)]
21. Zhang, J.; Zhu, Z.; Jiang, J.; Li, H. Fabrication of a novel AgI/LaFeO₃/g-C₃N₄ dual Z-scheme photocatalyst with enhanced photocatalytic performance. *Mater. Lett.* **2019**, *262*, 127029. [[CrossRef](#)]
22. Li, L.; Wang, H.; Wang, X. CeVO₄ nanofibers hybridized with g-C₃N₄ nanosheets with enhanced visible-light-driven photocatalytic activity. *Solid State Commun.* **2017**, *269*, 11–15. [[CrossRef](#)]
23. Chuaicham, C.; Karthikeyan, S.; Pawar, R.R.; Xiong, Y.; Dabo, I.; Ohtani, B.; Kim, Y.; Song, J.T.; Ishihara, T.; Sasaki, K. Energy-resolved distribution of electron traps for O/S-doped carbon nitrides by reversed double-beam photoacoustic spectroscopy and the photocatalytic reduction of Cr(vi). *Chem. Commun.* **2020**, *56*, 3793–3796. [[CrossRef](#)]
24. Balakumar, V.; Sekar, K.; Chuaicham, C.; Manivannan, R.; Sasaki, K. Synergistic ternary porous CN–PPy–MMt nanocomposite for efficient photocatalytic metronidazole mineralization: Performance, mechanism, and pathways. *Environ. Sci. Nano* **2021**, *8*, 2261–2276. [[CrossRef](#)]
25. Liu, Y.; Liu, H.; Zhou, H.; Li, T.; Zhang, L. A Z-scheme mechanism of N-ZnO/g-C₃N₄ for enhanced H₂ evolution and photocatalytic degradation. *Appl. Surf. Sci.* **2018**, *466*, 133–140. [[CrossRef](#)]
26. Huang, Y.; Zhang, X.; Zeng, J. Ternary heterojunctions catalyst of BiOCl nanosheets with the {001} facets compounded of Pt and reduced graphene oxide for enhancing photocatalytic activity. *J. Mater. Sci. Mater. Electron.* **2021**, *32*, 2667–2684. [[CrossRef](#)]
27. Sharma, G.; Kumar, A.; Sharma, S.; Al-Saeedi, S.I.; Al-Senani, G.M.; Nafady, A.; Ahamad, T.; Naushad, M.; Stadler, F.J. Fabrication of oxidized graphite supported La₂O₃/ZrO₂ nanocomposite for the photoremediation of toxic fast green dye. *J. Mol. Liq.* **2018**, *277*, 738–748. [[CrossRef](#)]

28. Ghosh, U.; Pal, A. Fabrication of a novel Bi₂O₃ nanoparticle impregnated nitrogen vacant 2D g-C₃N₄ nanosheet Z scheme photocatalyst for improved degradation of methylene blue dye under LED light illumination. *Appl. Surf. Sci.* **2019**, *507*, 144965. [[CrossRef](#)]
29. Fu, J.; Zhu, B.; Jiang, C.; Cheng, B.; You, W.; Yu, J. Hierarchical Porous O-Doped g-C₃N₄ with Enhanced Photocatalytic CO₂ Reduction Activity. *Small* **2017**, *13*, 1603938. [[CrossRef](#)]
30. Cao, S.; Liu, X.-F.; Yuan, Y.-P.; Zhang, Z.; Liao, Y.-S.; Fang, J.; Loo, J.; Sum, T.C.; Xue, C. Solar-to-fuels conversion over In₂O₃/g-C₃N₄ hybrid photocatalysts. *Appl. Catal. B Environ.* **2014**, *147*, 940–946. [[CrossRef](#)]
31. Yang, Y.; Guo, W.; Guo, Y.; Zhao, Y.; Yuan, X.; Guo, Y. Fabrication of Z-scheme plasmonic photocatalyst Ag@AgBr/g-C₃N₄ with enhanced visible-light photocatalytic activity. *J. Hazard. Mater.* **2014**, *271*, 150–159. [[CrossRef](#)] [[PubMed](#)]
32. Chuaicham, C.; Sekar, K.; Xiong, Y.; Balakumar, V.; Mittraphab, Y.; Shimizu, K.; Ohtani, B.; Dabo, I.; Sasaki, K. Single-step synthesis of oxygen-doped hollow porous graphitic carbon nitride for photocatalytic ciprofloxacin decomposition. *Chem. Eng. J.* **2021**, *425*, 130502. [[CrossRef](#)]
33. Xiang, Q.; Yu, J.; Jaroniec, M. Preparation and Enhanced Visible-Light Photocatalytic H₂-Production Activity of Graphene/C₃N₄ Composites. *J. Phys. Chem. C* **2011**, *115*, 7355–7363. [[CrossRef](#)]
34. Wang, S.; Wang, J. Magnetic 2D/2D oxygen doped g-C₃N₄/biochar composite to activate peroxydisulfate for degradation of emerging organic pollutants. *J. Hazard. Mater.* **2021**, *423*, 127207. [[CrossRef](#)]
35. Balakumar, V.; Ramalingam, M.; Sekar, K.; Chuaicham, C.; Sasaki, K. Fabrication and characterization of carbon quantum dots decorated hollow porous graphitic carbon nitride through polyaniline for photocatalysis. *Chem. Eng. J.* **2021**, *426*, 131739. [[CrossRef](#)]
36. Wu, T.; He, Q.; Liu, Z.; Shao, B.; Liang, Q.; Pan, Y.; Huang, J.; Peng, Z.; Liu, Y.; Zhao, C.; et al. Tube wall delamination engineering induces photogenerated carrier separation to achieve photocatalytic performance improvement of tubular g-C₃N₄. *J. Hazard. Mater.* **2021**, *424*, 127177. [[CrossRef](#)]
37. Sun, Y.; Hla, S.; Duffy, G.; Cousins, A.; French, D.; Morpeth, L.; Edwards, J.; Roberts, D. Effect of Ce on the structural features and catalytic properties of La_(0.9-x)Ce_xFeO₃ perovskite-like catalysts for the high temperature water–gas shift reaction. *Int. J. Hydrogen Energy* **2011**, *36*, 79–86. [[CrossRef](#)]
38. Tan, Y.; Ma, H.; Xiong, R.; Wei, J. Preparation and Photocatalytic Performance of Double-Shelled Hollow W₁₈O₄₉@C₃N₄@Ti₃C₂ Microspheres. *J. Wuhan Univ. Technol. Sci. Ed.* **2021**, *36*, 311–317. [[CrossRef](#)]
39. Yang, J.; Zhang, X.; Long, J.; Xie, C.; Wang, Y.; Wei, L.; Yang, X. Synthesis and photocatalytic mechanism of visible-light-driven AgBr/g-C₃N₄ composite. *J. Mater. Sci. Mater. Electron.* **2021**, *32*, 6158–6167. [[CrossRef](#)]
40. Wang, Y.; Di, Y.; Antonietti, M.; Li, H.; Chen, X.; Wang, X. Excellent Visible-Light Photocatalysis of Fluorinated Polymeric Carbon Nitride Solids. *Chem. Mater.* **2010**, *22*, 5119–5121. [[CrossRef](#)]
41. Jiang, X.; Liu, X.; Chen, Q.; Jin, R.; Lu, Y.; Yu, J.; Wu, Y.; He, Y. Preparation and Photocatalytic Activity of an Inorganic–Organic Hybrid Photocatalyst Ag₂WO₄/g-C₃N₄. *J. Inorg. Organomet. Polym. Mater.* **2017**, *27*, 1683–1693. [[CrossRef](#)]
42. Zhang, W.; Xu, C.; Liu, E.; Fan, J.; Hu, X. Facile strategy to construction Z-scheme ZnCo₂O₄/g-C₃N₄ photocatalyst with efficient H₂ evolution activity. *Appl. Surf. Sci.* **2020**, *515*, 146039. [[CrossRef](#)]
43. Chen, Q.; Zhao, C.; Wang, Y.; Chen, Y.; Ma, Y.; Chen, Z.; Yu, J.; Wu, Y.; He, Y. Synthesis of MoS₂/YVO₄ composite and its high photocatalytic performance in methyl orange degradation and H₂ evolution. *Sol. Energy* **2018**, *171*, 426–434. [[CrossRef](#)]
44. Zhang, J.; Zhang, M.; Sun, R.-Q.; Wang, X. A Facile Band Alignment of Polymeric Carbon Nitride Semiconductors to Construct Isotype Heterojunctions. *Angew. Chem. Int. Ed.* **2012**, *51*, 10145–10149. [[CrossRef](#)]
45. Ge, L.; Han, C.; Liu, J.; Li, Y. Enhanced visible light photocatalytic activity of novel polymeric g-C₃N₄ loaded with Ag nanoparticles. *Appl. Catal. A Gen.* **2011**, *409–410*, 215–222. [[CrossRef](#)]
46. Cao, G.; Li, Y.; Zhang, Q.; Wang, H. Synthesis and characterization of La₂O₃/TiO_{2-x}Fx and the visible light photocatalytic oxidation of 4-chlorophenol. *J. Hazard. Mater.* **2010**, *178*, 440–449. [[CrossRef](#)]
47. Ma, S.; Xue, J.; Zhou, Y.; Zhang, Z. Enhanced visible-light photocatalytic activity of Ag₂O/g-C₃N₄ p–n heterojunctions synthesized via a photochemical route for degradation of tetracycline hydrochloride. *RSC Adv.* **2015**, *5*, 40000–40006. [[CrossRef](#)]
48. Mao, W.; Wang, T.; Wang, H.; Zou, S.; Liu, S. Novel Bi₂WO₆ loaded g-C₃N₄ composites with enhanced photocatalytic degradation of dye and pharmaceutical wastewater under visible light irradiation. *J. Mater. Sci. Mater. Electron.* **2018**, *29*, 15174–15182. [[CrossRef](#)]
49. Wu, H.; Li, C.; Che, H.; Hu, H.; Hu, W.; Liu, C.; Ai, J.; Dong, H. Decoration of mesoporous Co₃O₄ nanospheres assembled by monocrystal nanodots on g-C₃N₄ to construct Z-scheme system for improving photocatalytic performance. *Appl. Surf. Sci.* **2018**, *440*, 308–319. [[CrossRef](#)]
50. Hong, Y.; Li, C.; Zhang, G.; Meng, Y.; Yin, B.; Zhao, Y.; Shi, W. Efficient and stable Nb₂O₅ modified g-C₃N₄ photocatalyst for removal of antibiotic pollutant. *Chem. Eng. J.* **2016**, *299*, 74–84. [[CrossRef](#)]
51. Li, C.; Yu, S.; Dong, H.; Liu, C.; Wu, H.; Che, H.; Chen, G. Z-scheme mesoporous photocatalyst constructed by modification of Sn₃O₄ nanoclusters on g-C₃N₄ nanosheets with improved photocatalytic performance and mechanism insight. *Appl. Catal. B Environ.* **2018**, *238*, 284–293. [[CrossRef](#)]
52. Xiao, T.; Tang, Z.; Yang, Y.; Tang, L.; Zhou, Y.; Zou, Z. In situ construction of hierarchical WO₃/g-C₃N₄ composite hollow microspheres as a Z-scheme photocatalyst for the degradation of antibiotics. *Appl. Catal. B Environ.* **2018**, *220*, 417–428. [[CrossRef](#)]

53. Chen, Q.; Yang, W.; Zhu, J.; Fu, L.; Li, D.; Zhou, L. Enhanced visible light photocatalytic activity of g-C₃N₄ decorated ZrO_{2-x} nanotubes heterostructure for degradation of tetracycline hydrochloride. *J. Hazard. Mater.* **2020**, *384*, 121275. [[CrossRef](#)] [[PubMed](#)]
54. Long, M.; Cai, W.; Cai, J.; Zhou, B.; Chai, X.; Wu, Y. Efficient Photocatalytic Degradation of Phenol over Co₃O₄/BiVO₄ Composite under Visible Light Irradiation. *J. Phys. Chem. B* **2006**, *110*, 20211–20216. [[CrossRef](#)]
55. Chang, X.; Huang, J.; Cheng, C.; Sui, Q.; Sha, W.; Ji, G.; Deng, S.; Yu, G. BiOX (X = Cl, Br, I) photocatalysts prepared using NaBiO₃ as the Bi source: Characterization and catalytic performance. *Catal. Commun.* **2010**, *11*, 460–464. [[CrossRef](#)]
56. Shen, C.-H.; Wen, X.-J.; Fei, Z.-H.; Liu, Z.-T.; Mu, Q.-M. Novel Z-scheme W₁₈O₄₉/CeO₂ heterojunction for improved photocatalytic hydrogen evolution. *J. Colloid Interface Sci.* **2020**, *579*, 297–306. [[CrossRef](#)]
57. Zeng, X.; Liu, L.; Lv, Y.; Zhao, B.; Ju, X.; Xu, S.; Zhang, J.; Tian, C.; Sun, D.; Tang, X. Ultra-sensitive and fast response formaldehyde sensor based on La₂O₃-In₂O₃ beaded nanotubes at low temperature. *Chem. Phys. Lett.* **2020**, *746*, 137289. [[CrossRef](#)]
58. Hua, S.; Qu, D.; An, L.; Jiang, W.; Wen, Y.; Wang, X.; Sun, Z. Highly efficient p-type Cu₃P/n-type g-C₃N₄ photocatalyst through Z-scheme charge transfer route. *Appl. Catal. B Environ.* **2018**, *240*, 253–261. [[CrossRef](#)]
59. Hu, L.; Hu, H.; Lu, W.; Lu, Y.; Wang, S. Novel composite BiFeO₃/ZrO₂ and its high photocatalytic performance under white LED visible-light irradiation. *Mater. Res. Bull.* **2019**, *120*, 110605. [[CrossRef](#)]
60. Ye, L.; Chen, J.; Tian, L.; Liu, J.; Peng, T.; Deng, K.; Zan, L. BiOI thin film via chemical vapor transport: Photocatalytic activity, durability, selectivity and mechanism. *Appl. Catal. B Environ.* **2013**, *130-131*, 1–7. [[CrossRef](#)]
61. Wang, X.; Zhang, L.; Lin, H.; Nong, Q.; Wu, Y.; Wu, T.; He, Y. Synthesis and characterization of a ZrO₂/g-C₃N₄ composite with enhanced visible-light photoactivity for rhodamine degradation. *RSC Adv.* **2014**, *4*, 40029–40035. [[CrossRef](#)]
62. Zhang, J.; Zhu, Z.; Jiang, J.; Li, H. Ultrasound-Assisted Hydrothermal Fabrication of AgI/MFeO₃/g-C₃N₄ (M = Y, Gd, La) Nano Sheet–Sphere–Sheet Photocatalysts with Enhanced Photodegradation Activities for Norfloxacin. *Catalysts* **2020**, *10*, 373. [[CrossRef](#)]
63. Li, D.; Shi, F.; Jiang, D.; Chen, M.; Shi, W. CdIn₂S₄/g-C₃N₄ heterojunction photocatalysts: Enhanced photocatalytic performance and charge transfer mechanism. *RSC Adv.* **2016**, *7*, 231–237. [[CrossRef](#)]
64. Liu, Y.; Kong, J.; Yuan, J.; Zhao, W.; Zhu, X.; Sun, C.; Xie, J. Enhanced photocatalytic activity over flower-like sphere Ag/Ag₂CO₃/BiVO₄ plasmonic heterojunction photocatalyst for tetracycline degradation. *Chem. Eng. J.* **2017**, *331*, 242–254. [[CrossRef](#)]